EES Catalysis

PAPER

View Article Online
View Journal

Check for updates

Cite this: DOI: 10.1039/d5ey00323g

Received 10th November 2025,
Accepted 16th January 2026

DOI: 10.1039/d5ey00323g

rsc.li/eescatalysis

Cooperative relay catalysis over Cu–Fe dual sites *via* N-intermediate and hydrogen radical pathways for ammonia production

Ming Zhang,[a] Zhiguo Li,[b] Zhipeng Ma,*[a] Constantine Tsounis,[a] Chen Han,[a] Shujie Zhou,[a] Wenyu Zhong,[a] Jitraporn Vongsvivut,[c] Jimmy Yun,[ad] Zhe Weng,[b] Jian Pan*[a] and Rose Amal[a]

Dual-atom catalysts (DACs) offer a powerful platform to investigate synergistic mechanisms in complex electrocatalytic reactions, yet direct experimental validation remains scarce. In this work, we present comprehensive evidence for a cooperative relay mechanism over a Cu–Fe DAC in the electrochemical reduction of nitrate (NO_3^-RR) to ammonia (NH_3). The spatially adjacent Cu and Fe atoms perform distinct but complementary roles: Cu sites facilitate NO_3^- activation and deoxygenation steps, while Fe sites drive stepwise hydrogenations through *H radical-assisted transfer. *In situ* Fourier-transform infrared (FTIR) spectroscopy, X-ray absorption spectroscopy (XAS), and electron paramagnetic resonance (EPR) collectively capture the evolution of N-containing intermediates and transient *H species, providing direct evidence for the dual-site relay pathway. This work elucidates the mechanistic underpinnings of DACs in NO_3^-RR and highlights cooperative site-specific catalysis as a promising design strategy for selective nitrogen conversion.

Broader context

This work advances the field of energy and environmental catalysis by establishing a comprehensive structure–performance relationship for CuFe dual-atom catalysts (DACs) in electrochemical nitrate reduction (NO_3^-RR). By integrating advanced *in situ*/*ex situ* characterizations with theoretical simulations, we uncover the cooperative catalytic roles of neighboring Cu and Fe sites that enable efficient nitrate activation and stepwise deoxygenation–hydrogenation toward ammonia. The CuFe DAC achieves a high faradaic efficiency of 94% and a remarkable NH_3 yield rate at low overpotential, far outperforming single-atom counterparts. Mechanistically, the synergistic Cu–Fe interactions optimize electronic structures, modulate *H dynamics, and suppress competing hydrogen evolution, thereby enhancing both selectivity and stability. These findings not only clarify the long-debated cooperative behavior in dual-site catalysis but also provide design principles for next-generation atomically dispersed catalysts. Beyond the fundamental advances, this work highlights the potential of electrocatalytic NO_3^-RR as a sustainable pathway for decentralized ammonia synthesis and wastewater remediation, addressing critical challenges in nitrogen cycle management and clean energy production.

1. Introduction

Heterogeneous catalysis serves as the basis for the modern chemical industry while playing a critical role in energy conversion and environmental remediation.[1,2] The development and optimization of single-atom catalysts (SACs) have gained significant attention due to their unique characteristics, including high surface energy, well-defined active sites, maximized atomic utilization, and tuneable electronic properties.[3,4] Inspired by these merits, numerous stable, cost-effective and efficient SACs (*e.g.* Fe, Co, Ni, Cu, Zn) have been developed for applications in organic synthesis, biomass valorization, electrocatalysis, energy production and storage applications, CO_2 conversion, methane to methanol, N_2 fixation, O_2 activation, CO conversion, and adsorption of toxic chemicals.[5–14] Considerable efforts have been devoted to engineering the microenvironment of SACs to achieve desired catalytic activity and selectivity.

In complex electrocatalytic reactions involving multiple intermediates, such as CO_2 reduction, nitrate reduction,

---

[a] *School of Chemical Engineering, The University of New South Wales, Kensington, New South Wales 2052, Australia. E-mail: zhipeng.ma@unsw.edu.au, jian.pan@unsw.edu.au*

[b] *Tianjin Key Laboratory of Advanced Carbon and Electrochemical Energy Storage, School of Chemical Engineering and Technology, and Collaborative Innovation Center of Chemical Science and Engineering, Tianjin University, Tianjin, 300072, China*

[c] *Infrared Microspectroscopy (IRM) Beamline, Australian Synchrotron, ANSTO, 800 Blackburn Road, Clayton, Victoria 3168, Australia*

[d] *Qingdao International Academician Park Research Institute, Qingdao, Shandong 266000, China*

nitrogen reduction, and oxygen reduction, the catalytic efficiency of SACs is often constrained by the inherent challenge of fine-tuning the adsorption energies of various intermediates. In such reactions, the adsorption behavior of one intermediate can impact the adsorption and reaction of others, making it difficult to optimize each step individually at a single active site.[15–20] This limitation presents a bottleneck in heterogeneous catalysis, especially in multi-step reactions where control of intermediate adsorption is crucial for both activity and selectivity. To overcome this challenge, binary metal catalysts have emerged as a promising solution to enhance the intrinsic activity of catalysts.[21–25] By introducing a second metal species, the adsorption and desorption behaviors of crucial intermediates can be regulated independently, resulting in decoupling of adsorption energies between species with different valencies and site binding preferences.[26,27]

Dual-atom catalyst (DAC), a type of binary metal catalyst, offers significant potential. By incorporating a second metal site adjacent to another metal site with short- or medium-range interaction, optimization of the microenvironment can be achieved.[28] The potential synergistic effects of DACs allow two metal sites to catalyze different core steps separately, improving overall catalytic performance. Additionally, the asymmetrical charge distribution on the heteronuclear dual-metal sites facilitates the simultaneous adsorption of intermediates, enhancing activity and selectivity while maintaining high atomic utilization efficiency and the good stability of SACs from strong metal-support interactions.[29] A recently-reported Cu/Fe diatomic catalyst synthesized on nitrogen-doped graphene exhibits good activity and selectivity for ammonia production, which is theoretically proved to provide a more favorable energy landscape for NO_3^- reduction to NH_3.[30] The absence of *in situ* experimental evidence leaves uncertainty regarding the exact catalytic pathway and intermediate stabilization. Furthermore, a study by Yang *et al.* explored Cu–Fe synergistic active sites (Cu–Fe/Fe_3C) for NO_3^- abatement targeting NO_3^--to-N_2 conversion.[31] This indicates that while CuFe DACs hold potential, their microenvironment and electronic structure must be carefully optimized to avoid undesired reaction pathways toward ammonia production.

To address these gaps, our work presents a systematic experimental and computational investigation of CuFe DACs, elucidating their catalytic roles and mechanistic advantages. *In situ* FTIR spectroscopy identifies the evolution of key nitrogen intermediates and distinguishes the adsorption–desorption behavior across dual metal sites, while the thermodynamic study quantifies NO_3^- activation energies, revealing the spatial advantage of CuFe dual sites supported by X-ray absorption (XAS) spectroscopy and DFT calculation. Beyond N-related intermediates, we explore the generation and consumption of $*H_{ads}$ intermediates through the kinetic study and electron paramagnetic resonance (EPR) spectroscopy, clarifying its role in balancing deoxygenation and hydrogenation. These insights establish a well-coordinated "relay catalysis mechanism", wherein Cu and Fe dual sites cooperatively facilitate NO_3^- activation and deoxygenation to *NO, and Fe sites promote subsequent hydrogenation to NH_3, collectively optimizing the reaction pathway. Herein, we report a CuFe DAC derived from a ZIF-8@M-ZnO (M: Cu and Fe) core-shell structure, achieving efficient, selective, and stable NO_3^- reduction to ammonia with a high faradaic efficiency (FE) of 94% at $-0.62\ V_{RHE}$ and a yield rate of 1757 μmol h^{-1} cm^{-2} (3514 μmol h^{-1} mg^{-1}) in electrolytes containing 1 M KOH and 1 M KNO_3. In addition, XAS and crystal orbital Hamilton population (COHP) analysis confirm strong Cu/Fe 3d–O 2p hybridization, lowering the free energy of NO_3^- adsorption. The observed shift in the rate-determining step (RDS) from NO_3^- adsorption in SACs to *NO hydrogenation in DACs further underscores the advantages of dual-site cooperation. This study introduces a high-performing and structurally robust CuFe DAC system and also advances the fundamental understanding of nitrate reduction through experimentally validated insights into dual-site catalysis, including kinetic differentiation of Cu and Fe roles, the critical involvement of H species, and electronic-level interactions, collectively offering a compelling strategy for rational DAC design.

2. Experimental

Synthesis of ZIF-8

A mixture containing 5.58 g of $Zn(NO_3)_2\cdot 6H_2O$ (Sigma Aldrich, 98%) and 6.16 g of 2-methylimidazole (Sigma Aldrich, 99%) was dissolved in 300 mL of methanol and subjected to ultrasonication for 5 minutes until it became cloudy. This mixture was then transferred to an oil bath heated to 120 °C and refluxed for 2 hours. Following cooling at room temperature, the resulting precipitate was collected *via* centrifugation and subsequently washed three times with methanol. Finally, approximately 1.45 g of white ZIF-8 powder was obtained after drying in a 60 °C vacuum oven for 6 hours.

Synthesis of Cu–ZnO, Fe–ZnO and bare ZnO

A mixture containing 1.1 g of $Zn(CH_3COO)_2\cdot 2H_2O$ (Sigma Aldrich, 98%) and either 50.5 mg of $Cu(CH_3COO)_2\cdot H_2O$ (Sigma Aldrich, 98%), or 44 mg of $Fe(CH_3COO)_2$ (Sigma Aldrich, 99.99%) was dissolved in 50 mL of DMSO (Dimethyl sulfoxide, Sigma Aldrich, 99.7%). Under vigorous stirring, 3.58 mL of tetramethylammonium hydroxide (Sigma Aldrich, 25 wt% in methanol) was added drop by drop. This was followed by the addition of 120 mL of ethyl acetate (Sigma Aldrich, 99.5%) while stirring continuously for an additional 10 minutes. The mixture was then left to stand, allowing the precipitate to settle, after which the supernatant was decanted until only 50 mL remained. The remaining mixture was centrifuged at 5000 rpm for 15 minutes to remove the clear liquid. The precipitate was then re-dispersed with 12 mL of ethanol, added in 4 mL increments, and ultrasonicated until it became transparent and evenly dispersed, yielding the desired Cu–ZnO and Fe–ZnO. For the bare ZnO, the same procedure was followed without the addition of the secondary metal acetate.

Synthesis of ZIF-8@M-ZnO

270 mg of ZIF-8 was dispersed in 27 mL of ethanol and vigorously stirred. A total of 3.6 mL of ZnO precursor solution was added, followed by continuous stirring for 12 hours. The

mixture was then centrifuged at 5500 rpm for 17 minutes to collect the sedimented product, which was subsequently dried under vacuum at 60 °C for 3 hours to yield the ZIF-8@M–ZnO product. The preparation of the target catalyst depends on the ZnO precursor recipe: for CuFe DACs synthesis, 2.4 mL of Cu–ZnO precursor solution and 1.2 mL of Fe–ZnO precursor solution were used to achieve an approximately 1 : 1 weight ratio of Cu to Fe in the obtained CuFe DACs; for Cu DACs synthesis, 2.4 mL of Cu–ZnO precursor solution and 1.2 mL of ZnO precursor solution were needed; and for Fe SACs, 2.4 mL of Fe–ZnO precursor solution and 1.2 mL of ZnO precursor solution were used.

Synthesis of CuFe DACs

160 mg of the ZIF-8@Cu/Fe–ZnO precursor was ground carefully for 30 minutes, and the fine powder was placed into a quartz boat and then into a tube furnace, in which nitrogen gas flow was introduced at a steady temperature of 50 °C for one hour. Gradually the temperature was elevated to 1000 °C at a controlled rate of 2 °C per minute and sustained for three hours forming CuFe DACs. Cu SACs, Fe SACs and N-doped carbon matrices were synthesized using the same method except using ZIF-8@Cu–ZnO, ZIF-8@Fe–ZnO, and ZIF-8@ZnO respectively.

Additional details about the electrochemical experiments, product quantifications, characterization methods, and computational methods are included in the SI.

3. Results and discussion

3.1. Synthesis and structural characterization

The fabrication of CuFe DACs follows a modified Zn-assisted atomization method, which is schematically illustrated in Fig. 1a.[32] Negatively charged ZIF-8 particles were used to carry positively charged Cu-doped ZnO nanoparticles (Cu–ZnO) and Fe-doped ZnO nanoparticles (Fe–ZnO), co-assembling them into a core–shell structure precursor (ZIF-8@Cu/Fe–ZnO) through electrostatic interactions in ethanol. Then, by calcining for 3 hours at 1000 °C in an N_2 atmosphere, an N-doped carbon matrix enriched by isolated Cu and Fe sites was obtained, referred to as CuFe DACs. For comparison, Cu SACs and Fe SACs were synthesized using the same method but instead by using Cu-doped ZnO or Fe-doped ZnO nanoparticles to obtain the respective precursors.

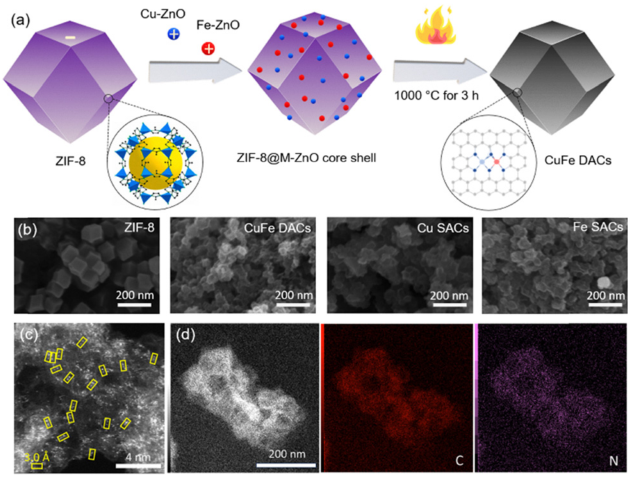

Fig. 1 (a) The two-step synthetic route of CuFe DACs. (b) SEM images showing the morphological evolution of ZIF-8 to CuFe DACs, Cu SACs, and Fe SACs. (c) AC HAADF-STEM image of CuFe DACs. (d) Corresponding EDS element mapping.

Scanning electron microscopy (SEM) images in Fig. 1b illustrate the morphological properties of ZIF-8, CuFe DACs, Cu SACs, and Fe SACs. It is noted that the rhombic dodecahedral morphological characteristic of ZIF-8 particles is inherited by CuFe DACs, Cu SACs, and Fe SACs, with a reduction in particle size from approximately 80 nm in ZIF-8 to about 40 nm. For the precursor of ZIF-8@M–ZnO (M = Cu or Fe), their larger average sizes (100–150 nm) compared to ZIF-8 particles can be seen in Fig. S1a–d with increased roughness on the surface, indicating the construction of a core–shell structure, *i.e.*, a ZIF-8 core covered by a metal-doped ZnO (M–ZnO) shell.[32] In the aberration-corrected high-angle annular dark-field scanning transmission electron microscope (AC HAADF-STEM images in Fig. 1c), isolated bright spots corresponding to heavy metal atoms suggest atomically dispersed Cu and Fe species on the N-doped carbon matrix. Notably, statistical analysis of the HAADF–STEM image (Fig. S2) shows that adjacent atomic pairs are mainly distributed within an interatomic distance range of 0.31–0.37 nm, representing approximately 79% of the total population, which supports the formation of dual sites. Furthermore, the energy-dispersive X-ray spectroscopy (EDS mapping in Fig. 1d) identifies the homogeneous distribution of carbon and nitrogen elements. No significant metal signals can be detected, likely due to the low concentration (Fig. S3 and S4). Inductively coupled plasma optical emission spectroscopy (ICP-OES) measurements indicate that the weight percentages of Cu and Fe in CuFe DACs are only 0.06% and 0.07%, respectively (Table S1).

The X-ray diffraction (XRD) pattern (Fig. S5) only shows two broad peaks around 23° and 42° (corresponding to the (002) and (100) crystal planes of graphite derived from the MOF ligand), further confirming that only detected crystalline phase is the graphitic carbon.[33,34] Raman spectroscopy (Fig. S6) reveals two distinct peaks, *i.e.*, the D band at approximately 1354 cm^{-1} and the G band at 1590 cm^{-1}. The two peaks are indicative of lattice defects and sp^2-hybridized carbon structures, respectively.[33,35–37] The ratio of the D band to the G band intensity (I_D/I_G) is a representation of the graphitization level of carbon materials. The consistency of the I_D/I_G ratio in CuFe DACs (0.90), Cu SACs (0.90), and Fe SACs (0.92) suggests that incorporating secondary metal atoms does not result in a significant amount of additional carbon defects on the surface of the catalyst.

3.2. Electronic structure of metal species

To ascertain the electronic properties of CuFe DACs, Cu SACs, and Fe SACs, the N 1s spectrum from XPS (X-ray photoelectron spectroscopy) was analyzed and fitted with five peaks (as shown in Fig. 2a and Fig. S7a and b, and Table S2) located at 398.4, 399.2, 400.5, 401.3, and 402.9 eV. These peaks are attributed to pyridinic N, metal–N, pyrrolic N, graphitic N, and oxidized N,

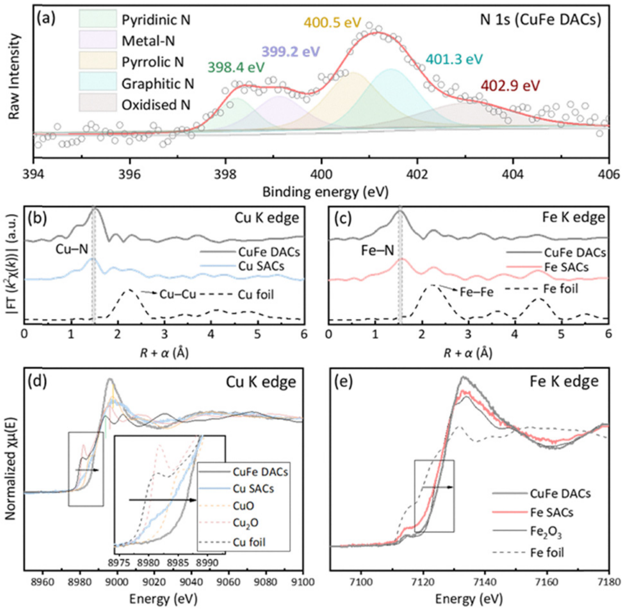

Fig. 2 (a) N 1s XPS spectrum of CuFe DACs. (b) Cu K-edge FT-EXAFS for CuFe DACs, Cu SACs and Cu foil shown in *R*-space. (c) Fe K-edge FT-EXAFS for CuFe DACs, Fe SACs and Fe foil shown in *R*-space (the data are k^2-weighted and not phase-corrected). (d) Cu K-edge XANES for CuFe DACs, Cu SACs, CuO standard, Cu_2O standard and Cu foil. (e) Fe K-edge XANES for CuFe DACs, Fe SACs, Fe_2O_3 standard and Fe foil.

respectively.[32,38] The presence of metal–N indicates that the single atoms are anchored to the N-doped carbon support *via* M–N bonding in the three catalysts. The Cu 2p and Fe 2p spectra were also collected (Fig. S6c and d). The characteristic peaks of 932.5 and 935.0 eV can be seen in Cu $2p_{3/2}$ XPS spectrum from Cu SACs, which can be assigned to Cu^+/Cu^0 and Cu^{2+} species, respectively.[39–41] The Fe 2p spectra showed a peak at around 711.3 eV (Fe $2p_{3/2}$) in both Fe SACs and CuFe DACs, corresponding to Fe^{3+} species.[42,43] However, the XPS signals of Cu 2p and Fe 2p spectra in CuFe DACs are too weak for further fitting analysis to understand the oxidation states of metal species. Therefore, XAS was utilized to provide further information about the oxidation states and coordination environment of Fe and Cu centers within CuFe DACs.

The EXAFS spectra of the Cu and Fe K-edge were collected to gain insight into the coordination environment around the metal centers. The k^2-weighted Fourier-transformed (FT) EXAFS Cu K-edge data (Fig. 2b) revealed a first shell peak at approximately 1.6 Å (without phase correction), indicative of a Cu–N bonding path, consistent with results observed from XPS analysis.[30,40] The absence of Cu–Cu bonding at 2.2 Å of the Cu K-edge spectrum together with the absence of Fe–Fe bonding at 2.2 Å of the Fe K-edge spectrum confirmed that the Cu and Fe species in CuFe DACs are atomically dispersed. The negligible metal–metal bonding in the Cu K-edge spectrum and Fe K-edge spectrum of Cu SACs and Fe SACs (Fig. 2b and Fig. S8), respectively, suggests that the coordination environment in Cu SACs and Fe SACs remains as Cu–N_x and Fe–N_x. These observations are further supported by the XANES spectrum (Fig. 2d and e), showing no obvious shift toward metallic foil characteristics.

The fitting results (Fig. S9 and Table S3) demonstrate an increase in Cu–N bond distance from 1.92 Å in Cu SACs to 1.96 Å in CuFe DACs, and an increase in the coordination number of Cu–N_x from 3.8 to 4.8. In contrast, the Fe K-edge FT-EXAFS (Fig. 2c) shows that the Fe–N bond distance remains nearly unchanged, with a slight variation from 2.03 Å in Fe SACs to 2.02 Å in CuFe DACs.[44] These results suggest that the introduction of dual Cu and Fe sites in DACs may result in the presence of a bridging N atom coordinating between Cu and Fe atoms. This bridging N could slightly alter the local electronic configuration and coordination environment,[45] leading to minimal variation in the Cu–N and Fe–N bond length due to local structural relaxation and/or electron redistribution in CuFe DACs (Fig. S10). Similarly, the coordination number of Fe–N_x increases from 3.4 in Fe SACs to 5.6, possibly due to the formation of a square pyramidal coordination geometry.[46] In this configuration, the metal center is surrounded by five ligand atoms, with four nitrogen (N) atoms occupying the corners of a square base and one ligand atom is positioned below the center of this base, forming a pyramid with a square base. Further insights of the X-ray absorption near-edge structure (XANES) spectrum (Fig. 2d and e) suggest that the fifth coordinating atom could be an oxygen (O) atom, likely from a hydroxyl group (–OH). This is supported by the positive shift observed in the edge positions and white line intensities in the Cu K-edge and Fe K-edge XANES spectra of CuFe DACs, compared to those of Cu SACs, Fe SACs, and the standard reference CuO and Fe_2O_3. This positive shift may be attributed to the formation of –OH, as $Cu(OH)_2$ was reported to exhibit a higher edge position than CuO.[47] As suggested in the literature, –OH can stabilize high-valence Cu and Fe centers under certain conditions, further supporting the observed changes in the XANES spectra. Thus, the edge shift likely results from a combination of increased oxidation states and –OH coordination.[48–50] In summary, EXAFS reveals that the Cu–N–Fe motif in CuFe DACs adopts a square pyramidal coordination geometry, while XANES suggests that the fifth ligand may be an –OH group. This unique coordination environment (HO–M–N_4), with adjacent Cu and Fe centers, likely enhances the adsorption of N-related intermediates through a synergistic effect, offering significant potential for improved performance in NO_3^-RR.

3.3. Electrochemical NO_3^-RR

The electrocatalytic nitrate reduction experiments were conducted in a typical three-electrode H-type cell with an electrolyte solution of 0.1 M KOH and 0.1 M KNO_3 (Fig. S11). Linear sweep voltammetry (LSV) depicted in Fig. 3a was initially employed to assess the catalysts' capability for NO_3^-RR. In the presence of KOH alone, electrocatalytic activity manifested in the hydrogen evolution reaction (HER). However, upon the addition of NO_3^-, a notable increase in current density was observed for both CuFe DACs and Cu SACs, with the onset potential shifting positively from about −0.4 V_{RHE} to roughly 0 V_{RHE}. For Fe SACs, while the addition of NO_3^- results in a minor positive shift in the onset potential, the magnitude of this shift is relatively limited. Additionally, at potentials more positive than −0.4 V_{RHE}, CuFe DACs and Cu SACs can achieve

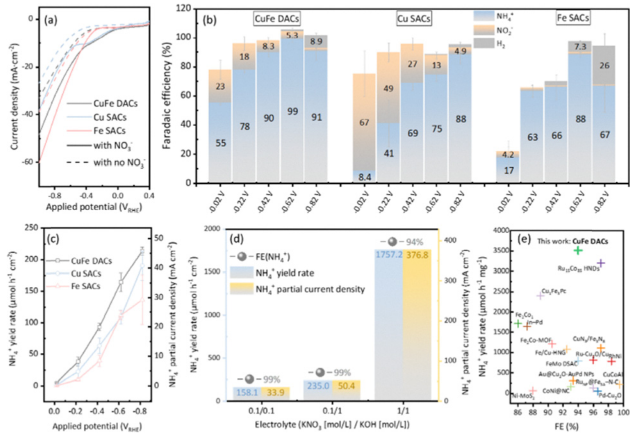

Fig. 3 (a) Linear sweep voltammetry (LSV) of CuFe DACs, Cu SACs, Fe SACs samples at a scan rate of 10 mV s^{-1} in an electrolyte of 0.1 M KOH with or without 0.1 M KNO_3. (b) FE of NH_4^+, NO_2^-, and H_2 in NO_3^-RR at varied potentials. (c) The yield rates (j) of NH_4^+ (left) and partial current density (right) at varied potentials. (d) FE and *j* for NH_4^+ in CuFe DACs-based NO_3^-RR at −0.62 V_{RHE} under various electrolyte concentrations, *i.e.*, 0.1 M KNO_3 and 0.1 M KOH, 0.1 M KNO_3 and 1 M KOH, 1 M KNO_3 and 1 M KOH. (e) Performance comparison of CuFe DACs and recently reported bimetallic electrocatalysts in NO_3^-RR.

higher current densities compared to Fe SACs. Specifically, CuFe DACs, Cu SACs, and Fe SACs require −0.33 V_{RHE}, −0.37 V_{RHE}, −0.42 V_{RHE}, respectively to reach a current density of 10 mA cm^{-2}. However, at more negative potentials (<-0.4 V_{RHE}), the current density of Fe SACs surpasses that of the other two catalysts, possibly due to the combined effects of nitrate reduction and HER. Thus, the exact proportion of electrons dedicated to NO_3^-RR *versus* HER necessitates quantitative product analysis to assess product selectivity and genuine catalytic activity for the conversion of nitrate to ammonia.

Therefore, the NO_3^-RR performance of CuFe DACs, Cu SACs, and Fe SACs was evaluated at varying potentials. As indicated in Fig. 3b, at −0.02 V_{RHE}, the Cu SACs system begins producing NH_4^+ and nitrite (NO_2^-), with nitrite being the dominant product ($FE_{NO_2^-}$ of 67%) and ammonia accounting for a FE of 8.4%. This could be due to the fact that most of the electrons being transferred to form the $*NO_2$ intermediate, which easily desorbs from the catalyst surface, preventing further multi-electron and proton-coupled reactions to form NH_4^+. Although the $FE_{NO_2^-}$ decreases as the potential becomes more negative, reaching 75% $FE_{NH_4^+}$ at −0.62 V_{RHE}, the highest $FE_{NH_4^+}$ observed is only 88% at −0.82 V_{RHE}. A similar trend is observed in the CuFe DACs system; however, it is noteworthy that at −0.02 V_{RHE}, most electrons are already directed towards ammonia synthesis, unlike the Cu SACs system, where the $*NO_2$ intermediate desorbs prematurely, halting further deoxygenation and hydrogenation steps necessary for NH_4^+ formation. As the applied potential becomes more negative, the $FE_{NH_4^+}$ increases from 55% at −0.02 V_{RHE} to a maximum of 99% at −0.62 V_{RHE}. Beyond this potential, the FE decreases slightly as the electron transfer begins to favor the hydrogen evolution reaction (HER). This suggests that in the CuFe DACs system, the introduction of a second Fe atom alters the adsorption mode or energy of the $*NO_2$ intermediate, or enhances $*H_{ads}$ availability as a reducing agent, promoting the continued NO_3^-RR towards the target product, NH_4^+.

To understand the advantages of Fe sites, Fe SACs were also tested for NO_3^-RR. At −0.02 V_{RHE}, nitrate reduction does not occur, and a more negative potential, such as −0.22 V_{RHE}, is required to initiate the reaction. As the potential becomes more negative, NH_4^+ emerges as the main product with minimal NO_2^- formation. The highest $FE_{NH_4^+}$ (88%) is achieved at −0.62 V_{RHE}, where HER also begins to compete. This suggests that while the Fe sites in Fe SACs effectively facilitate the NO_3^- to NO_2^- to NH_4^+ conversion, the reaction requires more negative potentials to start, possibly due to the weak adsorption of NO_3^- on Fe sites. This weak adsorption aligns with the subsequent analysis and highlights the need for stronger interaction between NO_3^- and active sites to lower the reaction onset potential.

From Fig. 3c, it is evident that all three catalyst systems exhibit an increasing trend in partial current density towards NH_4^+ production ($j_{NH_4^+}$) at increasingly negative potentials. Among them, CuFe DACs demonstrate superior performance, achieving a $j_{NH_4^+}$ of 35.2 mA cm^{-2} and yield rate of 164 ± 14 μmol h^{-1} cm^{-2} (328 ± 29 μmol h^{-1} mg^{-1}) at −0.62 V_{RHE} with highest turnover frequency (TOF in Fig. S12) of 12.3 s^{-1}. To evaluate whether this performance remains under various electrolyte conditions, we further tested NO_3^-RR in electrolyte containing 0.1 M KNO_3 and 1 M KOH (increased KOH concentration) and in electrolyte containing 1 M KNO_3 and 1 M KOH (increased KNO_3 and KOH concentration) at −0.62 V_{RHE} (Fig. 3d). When only the KOH concentration was increased tenfold, the $FE_{NH_4^+}$ remained as high as 99%, indicating that the alkaline environment did not compromise product selectivity. However, the $j_{NH_4^+}$ and yield rate improved only slightly from 33.9 to 50.4 mA cm^{-2} and from 158 to 235 μmol h^{-1} cm^{-2}, respectively. This minor enhancement may be attributed to increased proton availability and improved ionic conductivity. These results suggest that NO_3^- adsorption is the primary rate-limiting factor, and its surface coverage is not significantly affected by the KOH concentration alone. In contrast, when the NO_3^- concentration was also increased tenfold (to 1 M), the $FE_{NH_4^+}$ remained high at 94%, while both $j_{NH_4^+}$ and the yield rate increased over 11-fold to 376.8 mA cm^{-2} and 1757 μmol h^{-1} cm^{-2} (3514 μmol h^{-1} mg^{-1}), respectively. This implies that the low-concentration condition did not reach saturation coverage of NO_3^- on the catalyst surface, and that the balance between $*NO_3$ and $*H_{ads}$ adsorption remains well regulated even at high reaction rates. The capability to maintain high mass activity and high selectivity in 1 M KNO_3 and 1 M KOH at −0.62 V_{RHE} exhibits the advantage of CuFe DACs over previously reported bimetallic electrocatalysts (Fig. 3e).[30,51–65] To test the stability of the catalytic performance of CuFe DACs, a series of ten consecutive cyclic experiments were conducted (Fig. S13), which showed that $FE_{NH_4^+}$ could be maintained above 90% without significantly compromising the yield rate and partial current density. Furthermore, the Cu and Fe K-edges XANES and FT-EXAFS (Fig. S14) were measured for the CuFe DACs after the reaction. Comparing the XANES and FT-EXAFS spectra before and after the reaction revealed minimal changes to the oxidation state and coordination environment of metal active sites, demonstrating the chemical stability of Cu sites and Fe sites in CuFe DACs under electrocatalytic conditions. In addition, no metallic phases are observed in the XRD patterns (Fig. S15) after the reaction, which is consistent with the XRD pattern of pristine catalysts.

As the CuFe DAC is anchored on an N-doped carbon matrix, it is necessary to determine the nitrogen source in the produced ammonia. To this end, ^{15}N isotope labelling experiments were performed, with the resulting ammonium being characterized by ^{1}H nuclear magnetic resonance (^{1}H NMR) spectra, as depicted in Fig. S16. The ^{1}H NMR (600 MHz) spectra using $K^{15}NO_3$ as a reactant display the characteristic double peaks of $^{15}NH_4^+$, whereas those using $K^{14}NO_3$ exhibit the typical triple peaks of $^{14}NH_4^+$.[66] This distinct spectral evidence confirms that the nitrogen in the formed NH_4^+ originates exclusively from the nitrate ion in the electrolyte, rather than from the catalyst support. In addition, ^{1}H NMR was employed to validate the accuracy of the indophenol blue method for quantifying NH_4^+ *via* UV-vis spectroscopy. As shown in Fig. S17, the average deviation between the two methods was below 2%, indicating the reliability of the UV-vis approach. To rule out possible interference from Pt ion dissolution of Pt foil anode and redeposition at the cathode, we also performed control experiments using a graphite rod as the counter electrode. As shown in Fig. S18, no obvious changes were observed in either $FE_{NH_4^+}$ or $j_{NH_4^+}$, confirming the electrochemical stability of the Pt counter electrode and the negligible impact of Pt-derived species on the NO_3^-RR performance. In summary, the superior NH_4^+ production activity of CuFe DACs in NO_3^-RR is likely attributed to the optimized adsorption behavior of the $*NO_2$ intermediate at the Cu sites, which is enhanced by the presence of the second Fe atomic site, allowing it to achieve the benefits that can be obtained from both Cu and Fe systems. They exhibit higher product selectivity and catalytic activity, along with exceptional performance and chemical stability. This is attributed to the interaction of Cu and Fe center atoms in Cu–N–Fe motifs with optimized electronic structures, proving their potential value for practical applications.

3.4. Kinetic study and roles of $*H_{ads}$

To understand the superior catalytic activity and selectivity for ammonia production *via* nitrate reduction exhibited by CuFe DACs, the electrochemical active surface area (ECSA) of the catalysts was first characterized to discern the density of active sites on the surface. By conducting cyclic voltammetry (CV) within the non-faradaic potential region at various scan rates, the slope of the capacitive current density during charge–discharge processes, corresponding to the double-layer capacitance, was determined. As indicated in Fig. 4a and Fig. S19, and Table S4, the CuFe DACs exhibit the highest slope, translating to an ECSA of 1021 cm^2 (C_{dl} = 40.84 mF cm^{-2}), significantly surpassing that of Cu SACs and Fe SACs at 724 cm^2 (C_{dl} = 28.94 mF cm^{-2}) and 564 cm^2 (C_{dl} = 22.57 mF cm^{-2}), respectively. These results suggest that CuFe DACs offer more active sites, ensuring higher reaction activity and efficiency.[67]

Subsequently, the kinetics of the nitrate reduction reaction was investigated by performing electrochemical impedance spectroscopy (EIS) in the faradaic region where electrocatalytic reactions occur. The Nyquist plots and corresponding equivalent circuit fitting (Fig. 4b and Fig. S20) reveal the interfacial impedance of the three electrocatalysts, encompassing the electrolyte resistance (R_s), the charge transport resistance at the electrode–electrolyte interface (R_{CT1}), and the charge transfer resistance within the electrode (R_{CT2})—all of which are related to electrocatalytic kinetics.[68,69] A constant phase element (CPE) is typically employed to fit the non-ideal capacitance arising from surface inhomogeneity.[70] Notably, the electrolyte resistance (R_s) was essentially unaffected, remaining nearly identical for CuFe DACs, Cu SACs, and Fe SACs. However, the charge transport resistances at the electrode–electrolyte interface and within the electrode (R_{CT1} and R_{CT2}) respond to chemical changes at the interface.[71] The CuFe DACs displayed lower charge transport resistance (3.71 Ω for R_{CT1} and 11.7 Ω for R_{CT2}) compared to both Cu SACs (3.94 Ω for R_{CT1} and 23.9 Ω for R_{CT2}) and Fe SACs (5.25 Ω for R_{CT1} and 640 Ω for R_{CT2}). This reduction in resistance may be attributed to the CuFe DACs' stronger affinity towards the electrolyte, effectively minimising charge accumulation on the electrode surface and thereby facilitating a faster reaction rate with a smaller arc radius on the Nyquist plots' semicircle.

To elucidate the reason behind the CuFe DACs stronger affinity to charge transfer at the electrolyte interface, the apparent activation energy for different catalyst systems was measured through temperature-dependent partial current density experiments.[72] This parameter can be used to compare the minimum thermodynamic energy required for the specific reaction of nitrate reduction to ammonia, often inversely related to the reaction rate.[73] As shown in Fig. 4c and Table S5, the apparent activation energy for CuFe DACs is 14.3 kJ mol^{-1}, significantly lower than that of Cu SACs at 16.7 kJ mol^{-1} and Fe SACs at 18.5 kJ mol^{-1}. This indicates that the integration of Cu and Fe effectively lowers the energy barrier for the nitrate reduction to ammonia, facilitating easier adsorption and activation of nitrate ions at the electrode surface in the electrolyte,

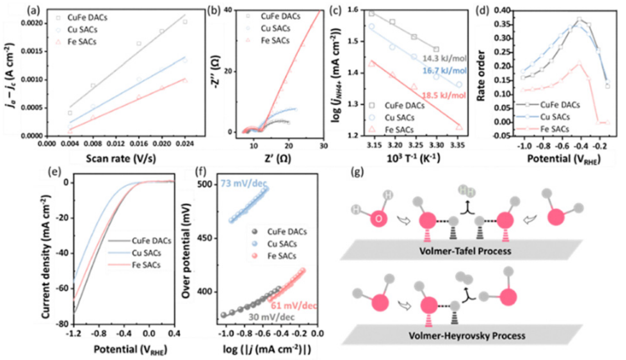

Fig. 4 (a) Capacitive current density as a function of scan rates. (b) EIS spectra. (c) T-dependant $j_{NH_4^+}$. (d) Potential-dependent reaction rate order. (e) LSV curve in 0.1 M KOH and (f) corresponding Tafel slope for HER on catalysts. (g) Schematic diagram of the Volmer–Tafel (top) and Vomer–Heyrovsky (bottom) processes on a catalyst surface.

which also explains the stronger binding affinity observed between the CuFe DACs electrode and the electrolyte.

For a comprehensive understanding of the kinetics of the NO_3^- reduction reaction (NO_3^-RR), steady-state chronoamperometry in 0.1 M KOH with varying concentrations of KNO_3 was employed (Fig. S21). The potential-dependent reaction order changes, as depicted in Fig. 4d, help infer the evolution and coverage state of the reactant substrate during the reaction in a wide potential window.[74] All catalysts underwent a process where the reaction order first increased and then decreased with more negative potentials, with peak values appearing at $-0.42\ V_{RHE}$. The reaction order of CuFe DACs reached the highest peak of approximately 0.37, while the reaction order of Fe SACs was the weakest at $-0.42\ V_{RHE}$, even with no reaction triggered at more positive potentials ($> -0.22\ V_{RHE}$), which is corresponding to the more negative onset potential required to initiate NO_3^-RR observed in Fig. 3a and b. This suggests that the CuFe DACs catalytic system has the fastest reaction rate at low biases, and at $-0.42\ V_{RHE}$, the reactant substrates $^*NO_3$ and *H have the most suitable coverage ratio on the electrode. However, as the potential becomes more negative, the catalyst surface may become increasingly covered by reaction intermediates, including adsorbed *H and *N-related species. This can lead to the saturation of active sites, limiting the availability of free sites for further adsorption. Consequently, the reaction order decreases as the surface becomes less responsive to changes in reactant concentration.[75] This potential-dependent trend is consistently observed within each individual catalyst system. Regarding the comparison between catalysts, particularly at potentials more negative than $-0.62\ V_{RHE}$, even the reaction order for the Cu SACs system surpasses that of CuFe DACs, which did not lead to better nitrate reduction activity towards NH_4^+. Instead, it may reflect the additional contribution from side reactions, such as NO_2^- formation and enhanced HER (*H–*H or *H–H_2O coupling), as shown by the increased FE_{H_2} and $FE_{NO_2^-}$ in Fig. 3b. These side reactions artificially elevate the overall reaction order without directly improving NH_4^+ production efficiency.

To clarify the contribution of the $^*H_{ads}$ in the electrocatalytic reduction of nitrate to ammonia and to explain the superior selectivity towards ammonia in the CuFe DACs system, LSV curves in 0.1 M KOH without NO_3^- (Fig. 4e) were examined for the three catalyst groups. The results indicated that CuFe DACs maintained a higher current density as the potential shifted negatively, and both CuFe DACs and Fe SACs exhibited earlier onset potentials than Cu SACs, suggesting more efficient HER activity in the CuFe DACs. Upon the introduction of 0.1 M KNO_3, the FE_{H2} in the CuFe DACs system was found to be suppressed compared to Fe SACs. This suppression could be due to the integration of Cu altering the direction of the reaction pathway, which is pivotal for both HER and NO_3^-RR, with $^*H_{ads}$ being an essential intermediate.

The Tafel slope analysis, which can elucidate the potential HER kinetics, was calculated by fitting the LSV curves to compare the reaction pathway differences in HER among the three catalysts by revealing the rate-determining step (RDS).[45,76] As depicted in Fig. 4f, the Tafel slope values for the catalysts are 30 mV dec^{-1} for CuFe DACs, 73 mV dec^{-1} for Cu SACs, and 61 mV dec^{-1} for Fe SACs. The reported Tafel slope of 30 mV dec^{-1} in HER suggests a Volmer–Tafel mechanism (illustrated in Fig. 4g), with the Tafel step being the rate-determining step (RDS).[77] This implies that the reaction pathway for CuFe DACs involves a water molecule adsorbing and dissociating at the site to form adsorbed hydrogen (Volmer step), followed by the relatively slower kinetic step of coupling two adsorbed hydrogens to produce a hydrogen molecule, with the Volmer step occurring more readily, accompanied by a higher *H generation rate. As the Tafel slope increases to approximately 40 mV dec^{-1}, the reaction pathway begins to shift towards a Volmer–Heyrovsky mechanism, a distinct pathway where the adsorbed hydrogen generated by the Volmer step directly reacts with a free water molecule to release hydrogen gas. As the slope further increases, as observed with Cu SACs and Fe SACs, the RDS begins to shift towards the Volmer step, indicating that the generation rate of $^*H_{ads}$ becomes the limiting factor for HER.[78,79] Therefore, the fast Volmer step of water dissociation ensures the superior *H generation rate at the active sites of CuFe DACs, which could also be the reason for the faster hydrogenation of the NO_3^--related substrate in nitrate reduction. Therefore, the HER analysis highlights the dual role of *H intermediates generated through optimized water dissociation on CuFe DACs *i.e.*, excessive *H formation favors HER side reaction, while the controlled and efficient utilization of *H can accelerate the hydrogenation and reduction of nitrate-related intermediates during NO_3^-RR.

To compare the behavior of *H species across different catalysts during NO_3^-RR, DMPO spin-trapping electron paramagnetic resonance (EPR) experiments were conducted at −0.62 V_{RHE} in 0.1 M KOH for CuFe DACs, Cu SACs, and Fe SACs. Control experiments with the addition of KNO_3 in 0.1 M KOH were also conducted (Fig. S22). In the absence of NO_3^-, Cu SACs and Fe SACs exhibited stronger DMPO–H signals than CuFe DACs, indicating more *H intermediate accumulation. The relatively weaker signal for CuFe DACs suggests faster *H consumption, likely due to more efficient *H–*H coupling and hydrogen evolution. However, upon the introduction of NO_3^- into the electrolyte, the trend reversed. Specifically, CuFe DACs showed an increase in DMPO–H intensity, while both Cu SACs and Fe SACs displayed significant decreases, resulting in weaker signals than those of CuFe DACs. The different signal intensity trend obtained with different electrolyte compositions highlight the distinct *H dynamics among the catalysts. Particularly, in SAC-based systems, the initially strong *H signal implies that *H species are readily generated but not effectively utilized, likely due to limited NO_3^- adsorption and activation. Consequently, after NO_3^- is introduced, the available *H is rapidly depleted, leading to a diminished EPR signal. In contrast, the increased DMPO–H signal observed for CuFe DACs after NO_3^- addition suggests a catalytic environment in which *H is both rapidly produced and consumed due to NO_3^- reduction as well as water dissociation, resulting in a transient accumulation of *H species that outpaces consumption. These findings align with the concentration-dependent activity trends shown in Fig. 3d, where increased NO_3^- concentration significantly enhances current density and ammonia yield. This improvement is not only attributed to faster NO_3^- adsorption, activation, and deoxygenation, but is also due to the net increase in *H species resulting from more efficient *H regeneration and a favorable balance between *H production and consumption. Overall, CuFe DACs sustain a dynamic and synergistic reaction environment that simultaneously supports high *H availability and efficient NO_3^- reduction, further reinforcing their advantage over SACs counterparts.

3.5. Catalytic mechanism

To elucidate the evolution process of the nitrate reactant into the target product ammonia, intermediates were tracked using *in situ* FTIR spectroscopy on CuFe DACs-based nitrate reduction reaction (NO_3^-RR) under increasing bias (see setup in Fig. S23). As shown in Fig. 5a, three downward absorption bands at 1127, 1380, and 1738 cm^{-1} emerged as the potential shifted negatively, corresponding to the N–O bond vibration, symmetric stretch, and bidentate coordination modes of NO_3^-, signifying the consumption of the NO_3^- substrate in the reaction.[80–82] Concurrently, the accumulation of the key intermediate *NO on the interface was evidenced by three peaks at 1529, 1675, and 1870 cm^{-1}.[83,84] Furthermore, as the potential shifted to −0.42 V_{RHE}, the emergence of bands at 1189 and 1430 cm^{-1} indicated the formation of species related to the terminal products, hydroxylamine (NH_2OH) and NH_4^+, respectively.[80,81] Simultaneously, the consumption of atomic $*H_{ads}$, indicated by the band centered at 2083 cm^{-1}, was observed in tandem with the formation of NH_2OH.[83] Although more negative potentials facilitate water dissociation and increase *H generation on the catalyst surface, this does not necessarily result in a stronger *H signal in the *in situ* FTIR spectra. This discrepancy arises because the FTIR signal intensity is governed by the net surface coverage of *H, which reflects the dynamic balance between its formation and consumption. At increasingly negative potentials, while *H formation accelerates, its consumption through subsequent hydrogenation steps becomes dominant. If the consumption rate surpasses the formation rate, the surface coverage, and thus the FTIR signal intensity may decrease, or the signal may even manifest as an inverted band. Based on these detected key intermediates, a reaction pathway for the electroreduction of nitrate to ammonia is proposed (illustrated at the top of Fig. 5b) as follows. Specifically, the nitrate is firstly activated at the electrode surface, undergoing two deoxygenation steps to form the *NO intermediate, followed by multiple hydrogenation steps on both N and O atoms by dissociated atomic H, leading to the formation of $*NH_2OH$ prior to the desorption of NH_3.

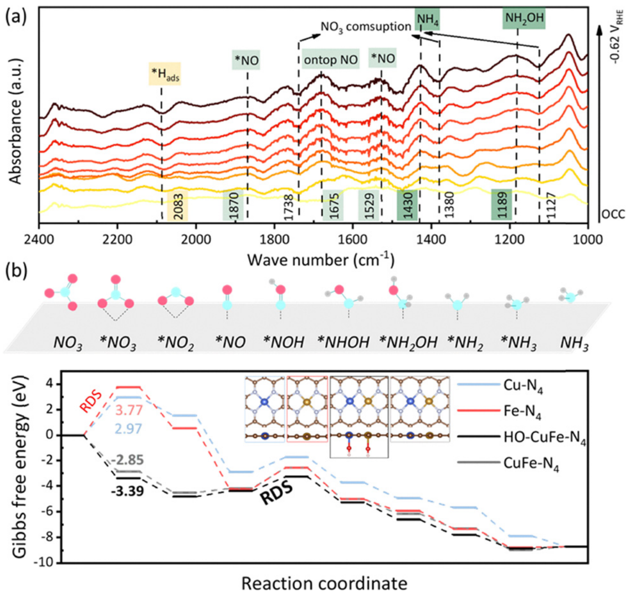

Fig. 5 (a) The *in situ* FTIR spectrum of CuFe DACs in NO_3^-RR *via* chronoamperometry polarization from open-circuit condition (OCC) to −0.62 V_{RHE}. (b) Gibbs free energy diagram of various intermediates generated during NO_3^-RR over the Cu–N_4, Fe–N_4, HO–CuFe–N_4, and CuFe–N_4. Blue, red, and grey balls represent N, O, and H atoms, respectively.

We also obtained the *in situ* FTIR spectra for Cu SACs and Fe SACs in NO_3^-RR as controls. Most of the key intermediates observed over CuFe DACs (*NO, $*NH_2OH$, and $*NH_4^+$, *etc.*) also appeared at similar wavenumbers in these SAC systems (Fig. S24a and b). In addition, a signal attributed to the antisymmetric stretching vibration of $*NO_2$ was also detected near 1240 cm^{-1}, with its intensity gradually increasing as the reaction progressed, indicating the accumulation of $*NO_2$ on the catalyst surface.[83] Moreover, notable changes in $*NO_3^-$-related signals over different catalysts were observed. Specifically, in CuFe DACs, the band at 1127 cm^{-1} showed a downward bend that became stronger with increasingly negative potential, suggesting that $*NO_3$ was being consumed faster than it accumulated. In contrast, in Cu SACs, the corresponding band at 1132 cm^{-1} showed a positive upward bend and remained nearly unchanged across the potential range, indicating a balance between $*NO_3$ accumulation and consumption. For Fe SACs, a similar upward bend appeared at ∼1127 cm^{-1}. Its intensity increased first and then slightly decreased at more negative potentials while remained slightly upward overall. This suggests that $*NO_3$ continued to accumulate, although the consumption rate temporarily increased before slowing again. Both SAC systems showed net $*NO_3$ accumulation during NO_3^-RR, while only CuFe DACs exhibited continuous and dominant $*NO_3$ consumption from the beginning. This demonstrates that CuFe DACs possess faster kinetics in the initial steps of the NO_3^-RR pathway, particularly in NO_3^- adsorption, activation, and deoxygenation to $*NO_2$.

Based on the reaction pathway revealed by *in situ* FTIR and the coordination environment obtained from EXAFS fitting, the surface models of the catalysts for the adsorption of each intermediate were constructed, representing the dual-atom pair configuration and isolated single-atom system. The changes in Gibbs free energy profiles were then determined through DFT calculations, as shown in Fig. 5b and Table S6. The optimized structure models of key NO_3^-RR intermediates are shown in Fig. S25–S28. It was found that in the initial step of nitrate adsorption and activation, the two single-atom catalysts (Cu–N_4 and Fe–N_4) require free energy changes of 2.97 eV and 3.77 eV, respectively. In contrast, this step occurs spontaneously in the dual-atom catalyst HO–CuFe–N_4 (−3.39 eV), favoring the formation of more activated *NO_3^- species *via* bidentate coordination mode. This finding aligns with apparent activation energy comparison (Fig. 4c) and explains the higher $j_{NH_4^+}$ and increased reaction activity observed over a wide potential window in CuFe DACs-based NO_3^-RR. Additionally, *NO_2^- adsorption on HO–CuFe–N_4 is the strongest among the three catalysts, preventing its desorption and thereby inhibiting the formation of *NO_2^-. This result is consistent with the experimental observation of a decreased FE of NO_2^- in Fig. 3b and explains the constrained FE of NO_2^-, ensuring the high selectivity of NH_4^+ production. Importantly, the reduction in the free energy changes for the first step leads to a shift in the rate-determining step (RDS) from the NO_3^- to * NO_3^- step in single-atom catalyst reactions to the *NO to *NOH step (the first hydrogenation step in nitrate reduction) in dual-atom catalyst reactions. Notably, the absorption energy of intermediates beyond *NO is not affected by the changes in adsorption energy from NO_3^- adsorption, indicating no cascading. This indicates that the inherent limitations of single-atom sites in Cu SACs or Fe SACs, particularly the consecutive formation and conversion of intermediates along with their associated adsorption energies, have been overcome. As a result, the reaction pathway, which originally had two uphill steps, is reduced to only one, thereby reducing the overall free energy span, accelerating the reaction dynamics, and enhancing NH_4^+ production. By allocating deoxygenation and hydrogenation to dual sites in dual active sites in CuFe DACs, the reaction pathway is effectively optimized through ‘‘cooperative relay catalysis’’, leading to improved efficiency. Regarding the roles of Cu sites and Fe sites in the CuFe DACs system, it is observed that from the *NO intermediate onwards, the continuous hydrogenation process (the role of *H_{ads} coverage was not investigated in calculation to simplify the modelling) leading to ammonia formation shows energy changes very consistent with those of Fe SACs. This alignment suggests that Fe sites have a preference for the hydrogenation process. The integration of Cu, however, significantly optimizes the adsorption of NO_3^- and its deoxygenation to form *NO. This could be due to the spatial advantage and system stability generated by the potential bidentate coordination of Cu–Fe dual sites with the two oxygen atoms in NO_3^-. Notably, the ‘‘cooperative relay mechanism’’ becomes evident during the generation of *NO, where only one O atom remains coordinated to a single site, enabling the distinct roles of Cu and Fe to come into effect. To demonstrate the general applicability of the dual-atom catalyst and its inherent advantages, a simplified CuFe–N_4 model with a planar square configuration (excluding the –OH ligand) is constructed. The calculated free energy profile of reaction intermediates shows that this model also enhances NO_3^- adsorption compared to SACs, although the improvement is less pronounced than that observed in the HO–CuFe–N_4 structure. Nevertheless, both CuFe–N_4 and HO–CuFe–N_4 models exhibit a similar downhill energy landscape, significantly outperforming the single-atom counterparts and reinforcing the effectiveness of dual-site relay catalysis.

To further elucidate the role of the fifth ligand, –OH, positioned below the center of the M–N_4 square base and its impact on the electronic structure–performance relationship, the crystal orbital Hamilton population (COHP) of NO_3 molecules adsorbed on HO–M–N_4 pyramids (Fig. 6a) was analyzed. This analysis is crucial for understanding how intermediates adsorb on a catalyst surface by revealing the interactions between atomic orbitals, where positive COHP values indicate antibonding contributions and negative values represent bonding contributions.[85] As shown in Fig. 6b, below the Fermi level (E_f), NO_3–(HO–CuFe–N_4) exhibits only a few antibonding contributions, while a significant increase in antibonding contributions is observed in models without –OH ligand, including NO_3–(CuFe–N_4), NO_3–(Cu–N_4), and NO_3–(Fe–N_4). To quantify the Metal–O bond strength, the integral of –COHP up to the Fermi level ($ICOHP_{Fermi}$) for NO_3–(HO–CuFe–N_4) was calculated to be −1.46, which is more negative than that of the other three models without –OH coordinated to the metal center (−1.09 for NO_3–(CuFe–N_4), −0.348 for NO_3–(Cu–N_4), and −0.623 for NO_3–(Fe–N_4)).[30,86] This indicates the strongest adsorption of NO_3 on HO–CuFe–N_4. This comparative approach supports our conclusion that the Cu site in the dual-atom configuration provides a distinct advantage in *NO_3 adsorption, which is a critical step toward achieving high catalytic efficiency.

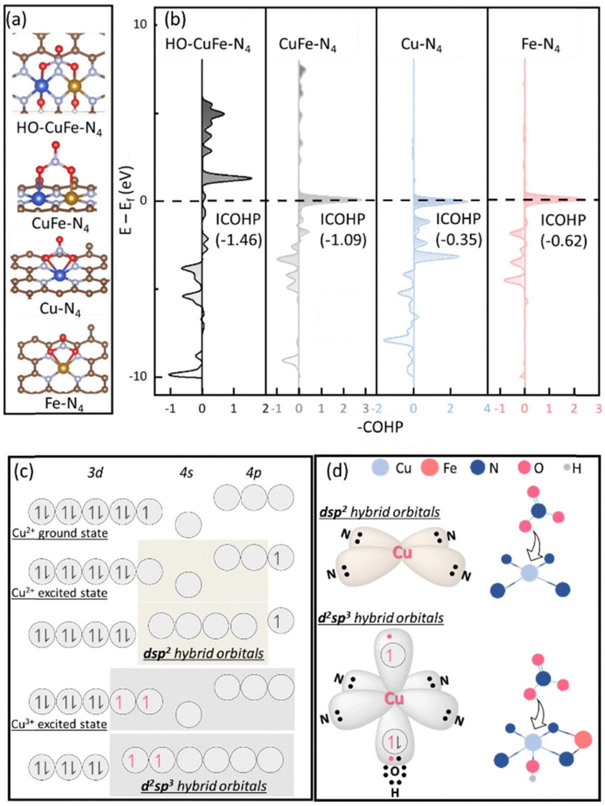

Fig. 6 (a) Optimized configurations of NO_3 adsorbed on HO–CuFe–N_4, CuFe–N_4, Cu–N_4, and Fe–N_4 for DFT calculations and (b) their corresponding COHP. (c) Illustration of the d_{sp^2} hybridization of Cu^{2+} in Cu SACs and d^2sp^3 hybridizations of Cu^{3+} in CuFe DACs. (d) NO_3 adsorption on the d_{sp^2} and d^2sp^3 Cu centers.

This observation can be understood based on the geometrical and electronic structure of HO–CuFe–N_4. Specifically, the Cu atom involves ten 3d electrons and one 4s electron in the valence shell.[87] When deposited on the N–C support to form Cu–N_4 SACs, the Cu atoms lose one 4s and one 3d electron, resulting in a four-coordinated Cu^{2+} ion.[88] Simultaneously, the unpaired $3d_{x^2-y^2}$_electron is excited to $4p_z$, while the unfilled $3d_{x^2-y^2}$, 4s, and 4p ($4p_x$, $4p_y$) orbitals undergo rearrangement to form planar square d_{sp^2} hybridized orbitals (Fig. 6c), which interact with the sp^2 orbitals of the four-coordinated N atoms (Fig. 6d).[89,90] Consequently, the remaining d orbitals of the supported Cu^{2+} ion are fully occupied. Specifically, this means the Cu^{2+} ion has a stable electronic configuration, with the d orbitals containing the maximum number of electrons, leaving no vacant d orbitals available for further bonding interactions. This stability reduces its reactivity toward adsorbing intermediates, such as nitrate. In contrast, when Cu is supported on N–C to form HO–Cu–N_4, as in CuFe DACs, the Cu atoms lose one 4s and two 3d electrons, resulting in an octahedral coordination environment for a Cu^{3+} ion *via* d^2sp^3 hybridization, with two unpaired electrons occupying two hybridized d^2sp^3 orbitals (Fig. 6c).[91] The formation of four Cu–N bonds and one Cu–OH bond leaves a half-filled d^2sp^3 orbital. As a result, NO_3 can gain these unpaired electrons and be activated more favorably when approaching the d^2sp^3-hybridized Cu center of HO–CuFe–N_4 (Fig. 6d), leading to substantial and strong NO_3 adsorption, as demonstrated by the COHP analysis.

Overall, these results reveal that the enhanced catalytic performance of CuFe DACs arises from a "cooperative relay catalysis" mechanism enabled by the unique spatial configuration of the carbon/nitrogen-coordinated dual-atom pair. The strong adsorption and activation of NO_3^- at the Cu site supported by orbital-level COHP analysis, facilitates efficient deoxygenation to *NO. This intermediate is subsequently hydrogenated at the Fe site to yield NH_4^+, a sequence that aligns well with the experimentally determined activation energy trend. This division of labor between Cu and Fe sites overcomes the limitations of isolated single-atom catalysts and enables an energetically favorable pathway with a reduced number of uphill steps. While these findings provide compelling evidence for the cooperative behavior of dual-metal sites, further advances could be achieved by employing atomic-level characterization techniques to directly probe the dual-site configuration, and by refining the synthesis strategy to increase the density and uniformity of Cu–Fe pairs. These efforts would further exploit the intrinsic advantages of DACs and push the boundaries of performance in selective nitrate reduction to ammonia.

4. Conclusions

In conclusion, a CuFe dual-atom catalyst was designed and synthesized using N-containing ZIF-8 as both a template and precursor. Compared to single-atom catalysts (Cu SACs and Fe SACs), the Cu and Fe metal pairs in CuFe DACs, with higher oxidation states and a unique geometric and electronic structure (HO–CuFe–N_4) revealed by XAS and supported by DFT calculations, exhibited enhanced activity and selectivity for NO_3^- reduction to NH_4^+. This improvement is attributed to stronger binding of $*NO_3$ and $*NO_2$, and a significant reduction in the overall free energy span of the reaction pathway. Specifically, the shift in the rate-determining step from $*NO_3$ adsorption in SACs to *NO hydrogenation in DACs facilitates a more energetically favorable reaction pathway, creating a more favorable energy landscape and accelerating NH_4^+ formation. This cooperative relay catalysis mechanism, where CuFe dual sites cooperatively facilitate $*NO_3$ deoxygenation while Fe sites drive *NO protonation, delivers high NH_4^+ yield rate of 1757 μmol h^{-1} cm^{-2} (3514 μmol h^{-1} mg^{-1}) with a 94% $FE_{NH_4^+}$ at −0.62 V_{RHE}. Furthermore, CuFe DACs exhibit an enhanced ability to dissociate water into H_{ads}, balancing the surface coverage of hydrogen radicals with N-intermediates, thereby sustaining the deoxygenation–hydrogenation relay. This work advances the design principles of DACs by providing a mechanistic understanding of active site cooperation, electronic reconfiguration, and reaction energetics. The integration of experimental and computational insights into catalytic mechanisms offers a pathway for developing highly selective and energy-efficient catalysts for NO_3^- reduction, contributing to sustainable ammonia production and broader applications in environmental remediation and clean energy conversion.

Author contributions

All authors contributed to the discussion and interpretation of the experiment and the completion of the manuscript. M. Z., C. H., S. Z., W. Z., and J. V. performed the experiments. Z. L. and Z. W. performed the theoretical calculation. M. Z., Z. L., Z. M., C. T., J. Y., Z. W., J. P., and R. A. performed the data analysis. M. Z., Z. M., J. P., and R. A. conceived the project. M. Z., Z. M., C. T., J. P., and R. A. drafted the manuscript. All authors have given approval to the final version of the manuscript.

Conflicts of interest

There are no conflicts to declare.

Data availability

The data supporting this article have been included as part of the supplementary information (SI). Supplementary information includes the experimental section with detailed experimental methods provided, supplementary Fig. S1–28, and supplementary Tables S1–6. See DOI: https://doi.org/10.1039/d5ey00323g.

Acknowledgements

The work was supported by the Australian Research Council (ARC) under the Discovery Early Career Researcher Award (DE190100131), ARC Training Centre for the Global Hydrogen Economy (GlobH2E, IC200100023), ARC Centre of Excellence for Carbon Science and Innovation (CoE-CSI, CE230100032), ARC Discovery Project (DP220102436), Australian Renewable Energy Agency (ARENA) Hydrogen R&D Funding Round under the Transformative Research Accelerating Commercialisation (TRAC) Program (ARENA PRO-1029).The authors acknowledge the ARC Discovery Project (DP220102436), GlobH2E, CoE-CSI, ARENA Pro-1029 for providing scholarship, instruments and characterization support, respectively. J.P., Z.M, and R.A. acknowledge UNSW-Tsinghua Collaborative Research Seed Program for support in catalyst evaluation. Z.M. acknowledges the fellowship program by the International Hydrogen Research Collaboration Program funded by Commonwealth Scientific and Industrial Research Organisation (CSIRO). The authors thank the Mark Wainwright Analytical Center at UNSW for providing characterization resources and training. The authors gratefully acknowledge the beamtime grants (AS233/MEX1/20550 and AS241/MEX1/21250) for synchrotron MEX1 beamtime at the Australian Synchrotron and extend their thanks to Dr. Emily Finch and Dr. Simon James for their invaluable assistance with the XAS experiments and discussions. Additionally, the authors acknowledge the beamtime grant (AS241/IRM/21262) for synchrotron IR beamtime at the Australian Synchrotron.

References

1 F. Zaera, *Chem. Rev.*, 2022, **122**, 8594–8757.

2 D. Chen, M. Sivakumar and A. K. Ray, *Dev. Chem. Eng. Mineral Process.*, 2008, **8**, 505–550.

3 D. B. Liu, Q. He, S. Q. Ding and L. Song, *Adv. Energy Mater.*, 2020, **10**, 2001482.

4 A. Q. Wang, J. Li and T. Zhang, *Nat. Rev. Chem.*, 2018, **2**, 65–81.

5 M. Li, S. J. Wu, X. Y. Yang, J. Hu, L. Peng, L. Bai, Q. S. Huo and J. Q. Guan, *Appl. Catal., A*, 2017, **543**, 61–66.

6 Y. Q. Zhu, W. M. Sun, W. X. Chen, T. Cao, Y. Xiong, J. Luo, J. C. Dong, L. R. Zheng, J. Zhang, X. L. Wang, C. Chen, Q. Peng, D. S. Wang and Y. D. Li, *Adv. Funct. Mater.*, 2018, **28**, 1802167.

7 F. Yang, P. Song, X. Liu, B. Mei, W. Xing, Z. Jiang, L. Gu and W. Xu, *Angew. Chem., Int. Ed.*, 2018, **57**, 12303–12307.

8 Y. Wang, F. Chu, J. Zeng, Q. Wang, T. Naren, Y. Li, Y. Cheng, Y. Lei and F. Wu, *ACS Nano*, 2021, **15**, 210–239.

9 S. Liu, H. B. Yang, S. F. Hung, J. Ding, W. Cai, L. Liu, J. Gao, X. Li, X. Ren, Z. Kuang, Y. Huang, T. Zhang and B. Liu, *Angew. Chem., Int. Ed.*, 2020, **59**, 798–803.

10 J. Yuan, W. Zhang, X. Li and J. Yang, *Chem. Commun.*, 2018, **54**, 2284–2287.

11 K. Niu, L. Chi, J. Rosen and J. Bjork, *J. Phys. Chem. Lett.*, 2022, **13**, 2800–2807.

12 Z. Y. Gao, W. J. Yang, X. L. Ding, G. Lv and W. P. Yan, *Phys. Chem. Chem. Phys.*, 2018, **20**, 7333–7341.

13 X. P. Zou, L. N. Wang, X. N. Li, Q. Y. Liu, Y. X. Zhao, T. M. Ma and S. G. He, *Angew. Chem., Int. Ed.*, 2018, **57**, 10989–10993.

14 Y. Monga, P. Kumar, R. K. Sharma, J. Filip, R. S. Varma, R. Zboril and M. B. Gawande, *ChemSusChem*, 2020, **13**, 3288–3305.

15 H. Ooka, J. Huang and K. S. Exner, *Front. Energy Res.*, 2021, **9**, 654460.

16 Z. Wang, D. Richards and N. Singh, *Catal. Sci. Technol.*, 2021, **11**, 705–725.

17 J.-X. Liu, D. Richards, N. Singh and B. R. Goldsmith, *ACS Catal.*, 2019, **9**, 7052–7064.

18 M. Yang, Z. Wang, D. Jiao, G. Li, Q. Cai and J. Zhao, *Appl. Surf. Sci.*, 2022, **592**, 153213.

19 E. M. Fernández, P. G. Moses, A. Toftelund, H. A. Hansen, J. I. Martínez, F. Abild-Pedersen, J. Kleis, B. Hinnemann, J. Rossmeisl, T. Bligaard and J. K. Nørskov, *Angew. Chem., Int. Ed.*, 2008, **47**, 4683–4686.

20 A. Kulkarni, S. Siahrostami, A. Patel and J. K. Nørskov, *Chem. Rev.*, 2018, **118**, 2302–2312.

21 Q. Gao, H. S. Pillai, Y. Huang, S. Liu, Q. Mu, X. Han, Z. Yan, H. Zhou, Q. He, H. Xin and H. Zhu, *Nat. Commun.*, 2022, **13**, 2338.

22 N. Sathishkumar and H.-T. Chen, *J. Phys. Chem. C*, 2023, **127**, 994–1005.

23 Y. Wang, A. Xu, Z. Wang, L. Huang, J. Li, F. Li, J. Wicks, M. Luo, D.-H. Nam, C.-S. Tan, Y. Ding, J. Wu, Y. Lum, C.-T. Dinh, D. Sinton, G. Zheng and E. H. Sargent, *J. Am. Chem. Soc.*, 2020, **142**, 5702–5708.

24 Z. Wang, S. D. Young, B. R. Goldsmith and N. Singh, *J. Catal.*, 2021, **395**, 143–154.

25 J. Cai, Y. Wei, A. Cao, J. Huang, Z. Jiang, S. Lu and S.-Q. Zang, *Appl. Catal., B*, 2022, **316**, 121683.

26 M. T. Darby, M. Stamatakis, A. Michaelides and E. C. H. Sykes, *J. Phys. Chem. Lett.*, 2018, **9**, 5636–5646.

27 D. R. Kanchan and A. Banerjee, *ChemSusChem*, 2023, **16**, e202300491.

28 Q. Wu, K. Chen, Z. Shadike and C. Li, *ACS Nano*, 2024, **18**, 13468–13483.

29 Q. Wang, Y. Cheng, H. B. Yang, C. Su and B. Liu, *Nat. Nanotechnol.*, 2024, **19**, 1442–1451.

30 S. Zhang, J. Wu, M. Zheng, X. Jin, Z. Shen, Z. Li, Y. Wang, Q. Wang, X. Wang, H. Wei, J. Zhang, P. Wang, S. Zhang, L. Yu, L. Dong, Q. Zhu, H. Zhang and J. Lu, *Nat. Commun.*, 2023, **14**, 3634.

31 Y. Hua, N. Song, Z. Wu, Y. Lan, H. Luo, Q. Song and J. Yang, *Adv. Funct. Mater.*, 2024, **34**, 2314461.

32 L. Jiao, J. Zhu, Y. Zhang, W. Yang, S. Zhou, A. Li, C. Xie, X. Zheng, W. Zhou, S.-H. Yu and H.-L. Jiang, *J. Am. Chem. Soc.*, 2021, **143**, 19417–19424.

33 J. Cheng, W. Sun, G. Dai, X. Yang, R. Xia, Y. Xu, X. Yang and W. Tu, *Fuel*, 2023, **332**, 126106.

34 B. Y. Xia, Y. Yan, N. Li, H. B. Wu, X. W. Lou and X. Wang, *Nat. Energy*, 2016, **1**, 15006.

35 X. Luo, X. Wei, H. Wang, W. Gu, T. Kaneko, Y. Yoshida, X. Zhao and C. Zhu, *Nano-Micro Lett.*, 2020, **12**, 163.

36 H.-J. Yang, J. Dong, Y.-H. Hong, W.-F. Lin, Z.-Y. Zhou and S.-G. Sun, *Electrochem. Commun.*, 2018, **97**, 82–86.

37 H. Chen, C. Zhang, L. Sheng, M. Wang, W. Fu, S. Gao, Z. Zhang, S. Chen, R. Si, L. Wang and B. Yang, *J. Hazard. Mater.*, 2022, **434**, 128892.

38 S. Zhuang, E. S. Lee, L. Lei, B. B. Nunna, L. Kuang and W. Zhang, *Int. J. Energy Res.*, 2016, **40**, 2136–2149.

39 A. M. Abdel-Mageed, B. Rungtaweevoranit, M. Parlinska-Wojtan, X. Pei, O. M. Yaghi and R. J. Behm, *J. Am. Chem. Soc.*, 2019, **141**, 5201–5210.

40 T. Yang, X. Mao, Y. Zhang, X. Wu, L. Wang, M. Chu, C.-W. Pao, S. Yang, Y. Xu and X. Huang, *Nat. Commun.*, 2021, **12**, 6022.

41 T. Zhang, X. Nie, W. Yu, X. Guo, C. Song, R. Si, Y. Liu and Z. Zhao, *iScience*, 2019, **22**, 97–108.

42 W. Liu, L. Zhang, X. Liu, X. Liu, X. Yang, S. Miao, W. Wang, A. Wang and T. Zhang, *J. Am. Chem. Soc.*, 2017, **139**, 10790–10798.

43 X. Xie, L. Peng, H. Yang, G. I. N. Waterhouse, L. Shang and T. Zhang, *Adv. Mater.*, 2021, **33**, 2101038.

44 Y. Pan, Y. Chen, K. Wu, Z. Chen, S. Liu, X. Cao, W.-C. Cheong, T. Meng, J. Luo, L. Zheng, C. Liu, D. Wang, Q. Peng, J. Li and C. Chen, *Nat. Commun.*, 2019, **10**, 4290.

45 Y. Chen, J. Lin, Q. Pan, X. Liu, T. Ma and X. Wang, *Angew. Chem., Int. Ed.*, 2023, **62**, e202306469.

46 Y. Pan, R. Lin, Y. Chen, S. Liu, W. Zhu, X. Cao, W. Chen, K. Wu, W.-C. Cheong, Y. Wang, L. Zheng, J. Luo, Y. Lin, Y. Liu, C. Liu, J. Li, Q. Lu, X. Chen, D. Wang, Q. Peng, C. Chen and Y. Li, *J. Am. Chem. Soc.*, 2018, **140**, 4218–4221.

47 C. E. Hendricks, A. N. Mansour, D. A. Fuentevilla, G. H. Waller, J. K. Ko and M. G. Pecht, *J. Electrochem. Soc.*, 2020, **167**, 090501.

48 S. Lu, X. Li, Y. Cheng, J. Zhou and G. Zhang, *Proc. Natl. Acad. Sci. U. S. A.*, 2023, **120**, e2306835120.

49 K. Keshari, A. Santra, L. Velasco, M. Sauvan, S. Kaur, A. D. Ugale, S. Munshi, J. F. Marco, D. Moonshiram and S. Paria, *JACS Au*, 2024, **4**, 1142–1154.

50 H. Kwon, J. Basran, C. M. Casadei, A. J. Fielding, T. E. Schrader, A. Ostermann, J. M. Devos, P. Aller, M. P. Blakeley, P. C. E. Moody and E. L. Raven, *Nat. Commun.*, 2016, **7**, 13445.

51 F. Lei, Y. Zhang, M. Xu, K. Li, M. Zhang, R. Huai, J. Xie, P. Hao, G. Cui and B. Tang, *ACS Sustainable Chem. Eng.*, 2023, **11**, 9057–9064.

52 Y. Xu, K. Ren, T. Ren, M. Wang, Z. Wang, X. Li, L. Wang and H. Wang, *Appl. Catal., B*, 2022, **306**, 121094.

53 J. Wan, H. Zhang, J. Yang, J. Zheng, Z. Han, W. Yuan, B. Lan and X. Li, *Appl. Catal., B*, 2024, **347**, 123816.

54 M. Xie, S. Tang, Z. Li, M. Wang, Z. Jin, P. Li, X. Zhan, H. Zhou and G. Yu, *J. Am. Chem. Soc.*, 2023, **145**, 13957–13967.

55 Y. Lv, S.-W. Ke, Y. Gu, B. Tian, L. Tang, P. Ran, Y. Zhao, J. Ma, J.-L. Zuo and M. Ding, *Angew. Chem., Int. Ed.*, 2023, **62**, e202305246.

56 S. Han, H. Li, T. Li, F. Chen, R. Yang, Y. Yu and B. Zhang, *Nat. Catal.*, 2023, **6**, 402–414.

57 J. Feng, Q. Hu, X. Yue, Q. Chen, C. Gao, J. Gu, L. Zhang, L. Zhang, H. Dai, F. Yang, G. Lin, K. P. Loh and Z.-X. Xu, *Appl. Catal., B*, 2025, **366**, 125027.

58 X. Yu, S. Du, Z. Xu, J. He, F. Liu, B. Wang, S. Sun, Y. Tang and K. Zhao, *Chem. Eng. J.*, 2024, **480**, 148152.

59 W. Zhong, Q.-L. Hong, X. Ai, C. Zhang, F.-M. Li, X.-F. Li and Y. Chen, *Adv. Mater.*, 2024, **36**, 2314351.

60 M. Yang, M. Chen, Y. Wang, J. Ma, L. Zhang, C. Hu, L. Zhuo, Y. Feng and X. Liu, *Commun. Chem.*, 2025, **8**, 267.

61 M. Yang, X. Hou, R. Fu, Z. Wang, C. Hu, G. Hu, L. Zhuo and X. Liu, *Nano Res.*, 2025, **18**, 94907778.

62 H. Guo, S. Tian, S. Luo, H. Wu, T. Li, G. Chen, X. Tu, W. Tian, C. Tang, G. Yang and Y. Zhou, *Appl. Catal., B*, 2026, **381**, 125865.

63 W. Wang, J. Chen and E. C. M. Tse, *J. Am. Chem. Soc.*, 2023, **145**, 26678–26687.

64 Y. Liu, X. Zhang, S. Feizpoor, H.-C. Chen, L. Li, Y. Zuo, S. Tian, M. Liu, W. Hu, M. Humayun, K. Huo, C. Lv, Y. Pang, D. Wang, X. Wang and C. Wang, *Adv. Mater.*, 2025, e14840.

65 J. Xu, H. Liu, S. Zhang, Q. Peng, S. Liu, J. Chen, X. Wang, W. Wang, H. Liu, Z. Xie, L. Song, K. Li and W. Chen, *J. Am. Chem. Soc.*, 2026, **148**(1), 148–161.

66 N. Zhou, Z. Wang, N. Zhang, D. Bao, H. Zhong and X. Zhang, *ACS Catal.*, 2023, **13**, 7529–7537.

67 H. Guo, M. Li, Y. Yang, R. Luo, W. Liu, F. Zhang, C. Tang, G. Yang and Y. Zhou, *Small*, 2023, **19**, 2207743.

68 Y. Kong, J. Li, Y. Wang, W. Chu and Z. Liu, *Catal. Lett.*, 2020, **150**, 3049–3057.

69 J. Zeng, K. Bejtka, W. Ju, M. Castellino, A. Chiodoni, A. Sacco, M. A. Farkhondehfal, S. Hernández, D. Rentsch, C. Battaglia and C. F. Pirri, *Appl. Catal., B*, 2018, **236**, 475–482.

70 J. Li, C. Du, Z. Liu and X. Li, *J. Mater. Sci. Technol.*, 2022, **118**, 208–217.

71 J. Gao, N. Shi, Y. Li, B. Jiang, T. Marhaba and W. Zhang, *Environ. Sci. Technol.*, 2022, **56**, 11602–11613.

72 W. Luo, S. Wu, Y. Jiang, P. Xu, J. Zou, J. Qian, X. Zhou, Y. Ge, H. Nie and Z. Yang, *ACS Appl. Mater. Interfaces*, 2023, **15**, 18928–18939.

73 M. Kumar and S. Chakraborty, *J. Hazard. Mater.*, 2006, **135**, 112–121.

74 Y. Wang, L. Zhang, Y. Niu, D. Fang, J. Wang, Q. Su and C. Wang, *Green Chem.*, 2021, **23**, 7594–7608.

75 Y. Wang, C. Wang, M. Li, Y. Yu and B. Zhang, *Chem. Soc. Rev.*, 2021, **50**, 6720–6733.

76 M. D. Makhafola, K. D. Modibane, K. E. Ramohlola, T. C. Maponya, M. J. Hato, K. Makgopa and E. I. Iwuoha, *Sci. Rep.*, 2021, **11**, 17219.

77 X. Tian, P. Zhao and W. Sheng, *Adv. Mater.*, 2019, **31**, 1808066.

78 S. Anantharaj, S. Noda, V. R. Jothi, S. Yi, M. Driess and P. W. Menezes, *Angew. Chem., Int. Ed.*, 2021, **60**, 18981–19006.

79 T. Shinagawa, A. T. Garcia-Esparza and K. Takanabe, *Sci. Rep.*, 2015, **5**, 13801.

80 K. Fan, W. Xie, J. Li, Y. Sun, P. Xu, Y. Tang, Z. Li and M. Shao, *Nat. Commun.*, 2022, **13**, 7958.

81 E. Pérez-Gallent, M. C. Figueiredo, I. Katsounaros and M. T. M. Koper, *Electrochim. Acta*, 2017, **227**, 77–84.

82 W. Wen, P. Yan, W. Sun, Y. Zhou and X.-Y. Yu, *Adv. Funct. Mater.*, 2023, **33**, 2212236.

83 J.-Y. Fang, Q.-Z. Zheng, Y.-Y. Lou, K.-M. Zhao, S.-N. Hu, G. Li, O. Akdim, X.-Y. Huang and S.-G. Sun, *Nat. Commun.*, 2022, **13**, 7899.

84 J. D. Schuttlefield, G. Rubasinghege, M. S. El-Maazawi, J. Bone and V. H. Grassian, *J. Am. Chem. Soc.*, 2008, **130**(37), 12210–12211.

85 Y. Zhang, C. Kang, W. Zhao, Y. Song, J. Zhu, H. Huo, Y. Ma, C. Du, P. Zuo, S. Lou and G. Yin, *J. Am. Chem. Soc.*, 2023, **145**, 1728–1739.

86 L. H. Zhang, Y. Jia, J. Zhan, G. Liu, G. Liu, F. Li and F. Yu, *Angew. Chem., Int. Ed.*, 2023, **62**, e202303483.

87 S. Pal, S. Sarkar, K. Kumar, R. Raghunathan, R. J. Choudhary, A. Banerjee and S. B. Roy, *Phys. Rev. B*, 2022, **105**, L060406.

88 M. Liu, J. Zhao, H. Dong, H. Meng, D. Cao, K. Zhu, J. Yao and G. Wang, *Small*, 2024, **20**, 2405309.

89 A. Jayamani, M. Sethupathi, S. O. Ojwach and N. Sengottuvelan, *Inorg. Chem. Commun.*, 2017, **84**, 144–149.

90 G. Tan and H. Zhu, *Inorg. Chem.*, 2011, **50**, 6979–6986.

91 Y. Cui, C. Ren, Q. Li, C. Ling and J. Wang, *J. Am. Chem. Soc.*, 2024, **146**, 15640–15647.